

Design and characterization of novel zirconium-based amorphous alloys containing scandium for biomedical application

Hai-Po Cui

University of Shanghai for Science and Technology

Wei-Dong Zhang

University of Shanghai for Science and Technology

Cheng-Li Song (✉ csong@usst.edu.cn)

University of Shanghai for Science and Technology

Original Article

Keywords: Amorphous alloy, Zirconium, Scandium, Mechanical property, Corrosion resistance

Posted Date: April 8th, 2021

DOI: <https://doi.org/10.21203/rs.3.rs-349393/v1>

License:  This work is licensed under a Creative Commons Attribution 4.0 International License.

[Read Full License](#)

Abstract

In this work, $(\text{Zr}_{55}\text{Cu}_{30}\text{Al}_{10}\text{Ni}_5)_{100-x}\text{Sc}_x$ ($x = 0, 0.5, 1.0, \text{ and } 1.5$) amorphous alloys were fabricated through steel die casting. The effects of scandium on the properties of zirconium-based amorphous alloys have been studied. The results show that the glass-forming ability of amorphous alloys increases at first and then decreases with the increase of Sc content. The highest glass-forming ability is obtained when the atomic fraction of Sc is 0.5%, which enables the production of 2-mm-thick amorphous alloy ingots. Meanwhile, the thermal stability and mechanical properties of the alloy are optimised with the atomic fraction of Sc of 1.0%. In addition, by adding an appropriate amount of Sc, the corrosion resistance of Zr–Cu–Al–Ni alloys is enhanced, particularly in the acid solution. The lowest average corrosion rate for samples in acid solution is obtained with the alloy containing atomic fraction of Sc of 1.0%. Therefore, results of this study indicate that the Zr-based amorphous alloy containing scandium has the potential for manufacturing fracture internal fixation or surgical devices.

1 Introduction

Amorphous alloy, also known as metallic glass, is a high-performance metallic material produced through solidification of metallic liquid into a non-crystalline form. Amorphous alloys possess uniform microstructures without crystal defects such as vacancies and grain boundaries[1–3]. Furthermore, amorphous alloys simultaneously exhibit metallic, glass, solid, and liquid properties due to the unique atomic structure. Despite showing the characteristics of metals amorphous alloys are capable of the free flowing and have self-repairing characteristic of glass within a specific temperature range[4–7]. Recently, amorphous alloys have been widely applied in engineering field due to their ultrahigh strength, hardness, elasticity, and corrosion resistance[8–10]. While in the medical field, Zr-based amorphous alloys show great application potential because the elastic modulus of Zr-based amorphous alloys is closer to that of human bones, making it suitable candidate material for orthopaedic applications.

Due to their structural characteristics, Zr-based amorphous alloys cannot be prepared by conventional methods, such as melting, forging and welding. At present, the preparation methods of bulk amorphous alloys include vacuum suction casting, water quenching, pressure model casting and so on. For the pressure model casting method, the broken master alloy ingot is put into the crucible and melted by high-voltage and high-frequency induction coil. Then the molten master alloy liquid is quickly pressed into the steel mould, and the rapid cooling is realized outside the steel mould through the water-cooling system. The filling speed and cooling rate of this method are very fast, and the high pressure is kept in the whole process, so it is easy to prepare bulk amorphous alloys. Furthermore, the higher filling pressure makes it possible to prepare amorphous alloy specimens with complex shapes.

The fabrication of zirconium-based amorphous alloys requires the purity of crystalline Zr with > 99.9%. The high price of this material limits the application of these alloys in aerospace and military engineering. Replacing ultrapure crystalline Zr with industrial-grade Zr sponge can substantially reduce production costs and critically affect the application of the amorphous alloys. Industrial-grade Zr sponge has high

hafnium and oxygen content. According to Inoue et al. from Tohoku University[11], Hf content of $\leq 15\%$ does not affect the glass-forming ability (GFA) of Zr-based amorphous alloys. Pajor et al. reported that GFA of Zr-based amorphous alloys is highly affected by oxygen content[12]. Zr oxides trigger heterogeneous nucleation-induced crystal phase formation, and substantially lower the critical dimension of the resultant alloys. Therefore, reducing or eliminating oxidation is critical to enhance the GFA of amorphous alloys fabricated by using Zr sponge. Many studies have demonstrated that adding trace amounts of other elements through microalloying can form more stable oxides with oxygen, thereby reducing or eliminating oxidation phenomenon in the process of preparing amorphous alloys and improving the critical dimension of a Zr-based amorphous alloys[13–15].

Scandium, the atomic number of 21, is a soft, silvery transition metal with the melting point of 1541°C and the boiling point of 2831°C . Sc has been employed in the production of special glass and lightweight heat-resistant alloy. In this study, industrial-grade Zr sponge was employed to fabricate $\text{Zr}_{55}\text{Cu}_{30}\text{Al}_{10}\text{Ni}_5$ amorphous alloys and the effects of trace amounts of Sc on the GFA, thermal stability, mechanical properties, and corrosion resistance of the alloy were investigated. The results are expected to help further expanding the application of Zr-based amorphous alloys in biomedical field.

2 Materials And Method

Zr sponge with the purity of 94% and copper, aluminium, nickel, and scandium with 99.9% purity were mixed according to the formula $(\text{Zr}_{55}\text{Cu}_{30}\text{Al}_{10}\text{Ni}_5)_{100-x}\text{Sc}_x$ ($x = 0, 0.5, 1.0, \text{ and } 1.5$). Under argon protection, the alloy was remelted three times using an electric arc melting furnace to ensure that the compositions of the master alloy ingot were evenly mixed. Figure 1 shows the sample of master alloy ingot. The master alloy ingot was taken out from the electric arc melting furnace and crushed by a hydraulic crusher. Then 150 g alloy fragments were weighed and placed in the EONTEC 500-C vacuum pressure rapid prototyping equipment (Fig. 2), and die casting was performed, with the amorphous alloy samples prepared at a mould temperature of 270°C , melting temperature of 990°C , and crucible heating current of 20–55 A. The dimension of each sample was 100 mm in length, 10 mm in width, and 1 mm or 2 mm in thickness, as shown in Fig. 3. The samples of $(\text{Zr}_{55}\text{Cu}_{30}\text{Al}_{10}\text{Ni}_5)_{100-x}\text{Sc}_x$ ($x = 0, 0.5, 1.0, 1.5$) alloys were coded as Zr01, Zr02, Zr03, and Zr04 according to the percentage of Sc content.

The phase structures of the samples were identified using a Rigaku X-ray diffractometer (Cu target, K_{α} radiation, 40 kV, 40 mA) at a scanning range of 20° – 80° , step size of 0.02° , and characteristic wavelength of 0.15405 nm. The energy spectra and fracture morphologies of the samples were obtained under a PhenomProx scanning electron microscope (SEM). To measure thermodynamic parameters, a DSC 404 F3 Phoenix differential scanning calorimeter was used at the heating rate of 20 K min^{-1} under argon protection. An Instron universal mechanical testing machine 5565 was employed to test the tensile and flexural properties of samples at room temperature with the tensile test speed of 2 mm min^{-1} , nonproportional elongation of 0.2%, and three-point flexural test span of 50 mm and speed of 10 mm min^{-1} . An HVS-1000 Vickers hardness tester was used to test the Vickers hardness of samples at the

load of 0.5 kg and load retention time of 10 s. The samples were immersed in 3 mol L⁻¹ HCl and NaOH solutions and NaCl solution with the mass fraction of 3.5% for 300 h to determine their corrosion rates.

3 Results And Discussion

3.1 Effect of Sc on the structure of the Zr-based alloys

3.1.1 X-ray diffraction (XRD) structural analysis

The diffraction intensities of X-rays are different when it interacts with various crystal phases in materials. Therefore, X-rays have long been applied in the analysis of the phase, texture, grain size, and microscopic stress of crystalline materials[16]. Unlike crystalline substances, amorphous substances exhibit nonordered long-range arrangement of particles and ordered short-range arrangement. Thus, they generate diffuse peaks when interacting with X-rays. Figure 4(a) shows the XRD pattern of the samples with 1 mm thickness. As we can see that normal amorphous diffuse peaks are present in the XRD curves of Zr02, Zr03, and Zr04 at $2\theta = 38^\circ\text{--}42^\circ$, and no crystalline diffraction peaks are found. At $2\theta = 40^\circ$, a few diffraction peaks are present in the Zr01 spectrum, indicating slight crystallisation.

Figure 4(b) shows the XRD pattern of the samples with 2 mm thickness. It can be seen that, at $2\theta = 38^\circ\text{--}42^\circ$, a typical diffuse peak of amorphous alloy is present in the Zr02 spectrum. A notable crystal diffraction peak is found in the diffuse peak of the Zr03 spectrum. The sharp diffraction peaks presenting in the Zr01 and Zr04 spectra indicates the substantial crystallisation. Accordingly, compared with the zirconium-based alloy without Sc, the sample with 0.5% Sc content exhibits considerably superior amorphousness at the critical dimension of 2 mm. However, the characteristic diffraction peaks increase in number and intensity with the Sc content increasing to higher than 0.5%, indicating an increase in the number of crystal phases in the samples. Consequently, the alloy is transformed from an amorphous structure to a composite structure with both amorphous and crystal phases.

Figure 4 reveals that Sc content has an important influence on the GFA of Zr-Cu-Al-Ni amorphous alloys, which increases at first and then decreases with the increase of Sc content. When the atomic fraction of Sc is 0.5%, i.e. Zr02, the GFA is optimised, enabling the production of 2-mm-thick amorphous alloy ingots.

3.1.2 SEM analysis

Figure 5 presents 5000× SEM images of the samples with 1 mm thickness. Some crystal phases can be observed in the amorphous base of Zr01. According to the energy spectrum analysis results presented in Table 1, the Al percentage of the crystal phases in Zr01 (16.87%) is higher than that of the amorphous base of Zr01 (8.67%). The Al content is thus 94.58% higher in the crystallised part of Zr01, indicating that the crystal phase in Zr01 is mainly formed by the enrichment and crystallization of Al.

As illustrated in Figures 5(b)-(d), bulk oxides of width >5 μm are present in the amorphous bases of Zr02, Zr03, and Zr04. According to the energy spectrum analysis results presented in Table 1, the sums of the Sc and O percentages of the three samples are all higher than 89%, indicating that Sc oxides are the primary substances in the amorphous bases. Accordingly, the Sc added to the Zr-Cu-Al-Ni amorphous alloys interacts with O during the melting process, forming Sc oxides and weakening the adverse effect of oxygen on glass-forming ability of amorphous alloys.

Table 1 Electron spectroscopy results

Analysis item	Atomic percentage (at.%)					
	Zr	Cu	Al	Ni	O	Sc
Zr01 amorphous base	49.87	28.30	8.67	4.82	8.33	-
Zr01 crystal phase	44.90	25.11	16.87	2.32	10.70	-
Zr02 oxide	5.09	2.78	0.88	0.35	58.40	32.49
Zr03 oxide	5.12	2.60	0.87	0.37	56.21	34.83
Zr04 oxide	5.96	3.36	0.93	0.29	60.96	28.50

3.2 Effect of Sc content on the thermal stability of the Zr-based alloys

Differential scanning calorimetry (DSC) determines, as a function of temperature, the amount of energy (per unit of time) required to heat a sample compared with that required to heat a reference material. In DSC experiment, the heat difference between a sample and reference material, which is caused by the endothermic or exothermic phase transition in the sample and is known as the compensation power, is measured to obtain the DSC curve of the sample, from which the sample's glass transition temperature, oxidation stability, crystallinity, chemical kinetics, enthalpy of fusion, and specific heat can be determined. To examine the effect of Sc on the thermal stability of the Zr-Cu-Al-Ni alloys, 20 mg of each sample (thickness = 1 mm) was tested to obtain its DSC curve. As shown in Figure 6, the DSC curves have obvious endothermic peaks caused by melting and exothermic peaks caused by crystallisation. Meanwhile, the tangent method was employed to calculate the glass transition temperature (T_g), initial crystallisation temperature (T_x), solidus temperature (T_m), and liquidus temperature (T_l) of the samples (Table 2). In addition, the reduced glass transition temperature ($T_{rg} = T_g/T_m$) and amorphous glass-forming ability [$\gamma = T_x / (T_g + T_l)$] of the samples were calculated. Generally, larger γ indicates that more energy is required for crystallisation; the stronger the crystallisation barrier of a sample, the more resistant the sample is against crystallisation and the higher its thermal stability is[17].

Table 2 Thermodynamic parameters of samples

Sample	T_g /K	T_x /K	T_m /K	T_l /K	T_{rg}	γ
Zr01	658.15	755.75	1097.45	1324.25	0.60	0.38
Zr02	675.25	755.75	1099.45	1237.25	0.61	0.39
Zr03	689.45	755.75	1101.55	1184.35	0.63	0.40
Zr04	689.85	743.05	1107.95	1197.05	0.62	0.39

As detailed in Table 2, T_{rg} and γ increase before decreasing with the increase of Sc content. Among the four samples, Zr03 exhibits the highest T_{rg} and γ , which are 0.63 and 0.40, respectively, indicating that the thermal stability of the Zr-Cu-Al-Ni-Sc amorphous alloys is highest with the atomic fraction of Sc of 1.0%.

3.3 Effect of Sc content on the mechanical properties of the Zr-based alloys

3.3.1 Hardness test

Hardness refers to the resistance of a material to pressure from another material. It is a critical mechanical indicator for an amorphous alloy. Vickers hardness is calculated as follows:

$$\begin{aligned} \text{Vickers hardness} &= 0.102 \times \frac{\text{test force}}{\text{indentation surface area}} \\ &= \frac{0.102(2F \sin 68^\circ)}{d^2} \approx 0.1891 \frac{F}{d^2} \quad (1) \end{aligned}$$

The Vickers hardness of 1-mm-thick sample was tested at the load of 0.5 kg and load retention time of 10 s. Each sample had its surface scratches removed, and five load points on the surface were randomly selected to test the diagonal lengths of their indentation. The aforementioned formula was then used to calculate the

Vickers hardness of the load points, and the mean hardness value was determined as shown in Table 3. The results reveal that Zr03 (1.0% Sc) had the highest Vickers hardness (469.2 HV).

Table 3 Vickers hardness of samples

Sample	Zr01	Zr02	Zr03	Zr04
Hardness (HV)	460.7	463.8	469.2	467.9

3.3.2 Tensile testing

Figure 7 and Figure 8 depict the uniaxial tensile conditions and tensile stress–strain curves of the samples, respectively. It can be seen from the Figure 8 that the samples fracture rapidly after elastic deformation in the tensile process. There is no plastic deformation stage of crystalline materials, which shows the brittle fracture characteristic of amorphous alloys.

According to the tensile testing results (Table 4), the tensile strength of samples increases at first and then decreases with the increase of Sc content. When the atomic fraction of Sc is 1.0%, the tensile strength of the alloy and its elongation at break are at their highest values of 1437.73 MPa and 2.92%, respectively.

Table 4 Tensile testing results

Sample	Tensile strength (MPa)	Maximum force (N)	Elongation at break (%)
Zr01	1235.15	6217.74	2.59
Zr02	1260.90	6304.52	2.61
Zr03	1437.73	7189.76	2.92
Zr04	1339.60	6698.00	2.73

As we can see from Table 3 and Table 4, resembling that of crystalline materials, a linear relationship exists between strength and hardness for amorphous alloys. Zr03 exhibits the highest tensile strength and Vickers hardness.

Generally, the plastic deformation of amorphous alloy caused by trace elements is precipitated by endogenous nanoparticles in the amorphous matrix obstructing the slippage of shear bands[18]. As revealed in the present experiment, increasing the trace amount of Sc cannot enhance the plastic-deformation-related mechanical properties of the Zr-Cu-Al-Ni alloy, which still reflects the brittleness of the amorphous alloy at room temperature. Figure 9 reveals the morphologies of the tensile fractures of samples. Numerous river-shaped veins can be observed in the Zr03 fracture, which are caused by a rapid temperature rise in the highly localised shear band at break as well as the viscous flow during the fracture. Accordingly, considerable energy is required to generate and expand a shear band, which could explain the impressive strength of the amorphous alloy.

3.3.3 Three-point flexural test

In the specification of $100 \times 5 \times 1 \text{ mm}^3$, the four samples were subjected to the three-point flexural test at a 50 mm span. The flexural test data are listed in Table 5. Figure 10 plots the flexural strength and flexural modulus against the atomic fraction of Sc.

As we can see that the flexural strength and modulus of the Zr-Cu-Al-Ni alloy increases at first and then decreases with the increase of Sc content. Of all four samples, Zr03 exhibits the highest flexural strength (2236.72 MPa) and modulus (74.69 GPa). Therefore, the Vickers hardness, tensile strength and flexural strength of the Zr-Cu-Al-Ni alloy are the highest and the comprehensive mechanical properties are the best with the atomic fraction of Sc of 1.0%.

Table 5 Flexural testing data

Sample	Flexural strength (MPa)	Flexural modulus (GPa)
Zr01	2094.37	72.86
Zr02	2111.40	73.98
Zr03	2236.72	74.69
Zr04	2048.62	74.04

3.4 Effect of Sc content on the corrosion resistance of the Zr-based alloys

The four samples with the dimension of $10 \times 10 \times 1$ mm were subjected to a corrosion resistance test. They were cleared of surface scratches using 800#, 1000#, 1200#, and 1500# mesh sandpaper before cleaned, dried, and weighed. The samples were then placed inside 3-mol L^{-1} HCl and NaOH solutions and NaCl solution with 3.5% mass fraction in a fume hood at the room temperature and atmospheric pressure for 300 h. Strong reactions were noted after the samples had been present in the HCl solution for 200 h, as indicated by corrosion cracks. A large amount of microbubbles emerged from the cracks and were followed by black oxides. After 300 h of immersion, a small amount of white flocculi was generated. However, no notable reactions were detected in the NaOH and NaCl solutions. After the test, the samples were cleaned, dried, and weighed. The weight changes of the samples were identified, and the average corrosion rates were calculated as follows:

$$v = \frac{W_0 - W_1}{S \times t} \quad (2)$$

where W_0 and W_1 indicate the masses before and after corrosion, respectively; S indicates the surface area of sample; t represents the immersion period; v represents the average corrosion rate ($\text{g m}^{-2} \text{h}^{-1}$).

Table 6 lists the average corrosion rates of the samples in HCl, NaOH, and NaCl solutions. Although the HCl and NaCl solutions have equal chlorine concentrations, the samples are corroded considerably faster in the HCl solution than in the NaCl solution. The result reveals that chlorine ions exerted negligible or no effect on the corrosion of the $(\text{Zr}_{55}\text{Cu}_{30}\text{Al}_{10}\text{Ni}_5)_{100-x}\text{Sc}_x$ ($x = 0, 0.5, 1.0, 1.5$) amorphous alloys.

Table 6 Corrosion test results

Sample	Average corrosion rate ($\text{g m}^{-2} \text{h}^{-1}$)		
	HCl	NaOH	NaCl
Zr01	0.5986	0.0014	0.0069
Zr02	0.3278	0	0
Zr03	0.1444	0	0.0014
Zr04	2.5250	0	0

Results shown in Figure 11 indicate that the alloys corrode more quickly in the acid solution. The average corrosion rate of the alloys decreases at first and then increases with the increase of Sc content. The corrosion resistance of the alloys is the highest with the atomic fraction of Sc of 1.0%. Moreover, the corrosion resistance of the sample immersed in NaOH and NaCl solutions is slightly enhanced with the addition of Sc. Accordingly, proper addition of Sc is beneficial to improve the corrosion resistance of Zr-Cu-Al-Ni alloys.

4 Conclusions

In summary, we have developed a series of new $(\text{Zr}_{55}\text{Cu}_{30}\text{Al}_{10}\text{Ni}_5)_{100-x}\text{Sc}_x$ ($x = 0, 0.5, 1.0, \text{ and } 1.5$) amorphous alloys and characterized them with XRD, DSC, mechanical property and corrosion tests. Results of this study indicate that Sc content has an important influence on the GFA of Zr–Cu–Al–Ni amorphous alloys, which increases at first and then decreases with the increase of Sc content. When the atomic fraction of Sc is 0.5%, the GFA is optimised, enabling the production of 2-mm-thick amorphous alloy ingots. The thermal stability and comprehensive mechanical properties of the alloy are the best with the atomic fraction of Sc of 1.0%. Specifically, the Vickers hardness, tensile strength, and flexural strength are maximised at 469.2 HV, 1437.73 MPa, and 2236.72 MPa, respectively. By adding an appropriate amount of Sc, the corrosion resistance of Zr–Cu–Al–Ni alloys is enhanced, particularly in the acid solution. The lowest average corrosion rate for samples in acid solution is obtained with the alloy containing atomic fraction of Sc of 1.0%. Therefore, it has the potential to be used in the medical field as the material for manufacturing fracture internal fixation or surgical devices.

Declarations

Funding

Supported by National Natural Science Foundation of China (Grant No. 51735003), and Shanghai Natural Science Foundation of China (Grant No. 19ZR1435300).

Availability of data and materials

The datasets supporting the conclusions of this article are included within the article.

Authors' contributions

The author' contributions are as follows: Hai-Po Cui and Wei-Dong Zhang were in charge of the whole trial; Cheng-Li Song assisted with sampling and laboratory analyses.

Competing interests

The authors declare no competing financial interests.

Consent for publication

Not applicable

Ethics approval and consent to participate

Not applicable

References

1. C Y Li, J F Yin, J Q Ding, et al. Effect of Er on properties of Zr-based bulk metallic glasses. *Materials Science and Technology*, 2018, 34(15): 1887-1892.
2. M Yan, J Zou, J Shen, et al. Compositional design and microstructure analysis of Zr-based bulk metallic glasses. *Transactions of Nonferrous Metals Society of China*, 2007, 17(6): 1433-1440.
3. M Rahvard, M Tamizifar, S M Boutorabi. Zr-Co(Cu)-Al bulk metallic glasses with optimal glass-forming ability and their compressive properties. *Transactions of Nonferrous Metals Society of China*, 2018, 28(8): 1543-1552.
4. S S Chen, J X Tu, J J Wu, et al. Phase separation and significant plastic strain in a Zr-Cu-Ni-Al-Fe bulk metallic glass. *Materials Science & Engineering A*, 2016, 656(2): 84-89.
5. N Nollmann, I Binkowski, V Schmidt, et al. Impact of micro-alloying on the plasticity of Pd-based bulk metallic glasses. *Scripta Materialia*, 2015, 111(6): 119-122.
6. M Yang, X J Liu, Y Wu, et al. Elastic modulus change and its relation with glass-forming ability and plasticity in bulk metallic glasses. *Scripta Materialia*, 2019, 161(3): 62-65.
7. P Gong, S B Wang, Z Liu, et al. Lightweight Ti-based bulk metallic glasses with superior thermoplastic formability. *Intermetallics*, 2018, 98(7): 54-59.
8. M Rahvard, M Tamizifar, S M Boutorabi. Enhanced plasticity of $Zr_{56}Co_{24}Ag_4Al_{16}$ and $Zr_{56}Co_{22}Cu_6Al_{16}$ bulk metallic glasses by controlling the casting temperature. *Journal of Non-Crystalline Solids*, 2018, 491(7): 114-123.
9. L Kramer, Y Champion, K S Kormout, et al. Bulk metallic dual phase glasses by severe plastic deformation. *Intermetallics*, 2018, 94(3): 172-178.
10. X Ma, Q Li, L Chang, et al. Enhancement on GFA and mechanical properties of Ni-based bulk metallic glasses through Fe addition. *Intermetallics*, 2017, 90(11): 58-62.
11. A Inoue, T Shibata, T Zhang. Effect of additional elements on glass transition behavior and glass formation tendency of Zr-Al-Cu-Ni alloys. *Materials Science & Engineering A*, 1995, 36(12): 1420-1426.
12. K Pajor, T Koziel, G Cios, et al. Glass forming ability of the $Zr_{50}Cu_{40}Al_{10}$ alloy with two oxygen levels. *Journal of Non-Crystalline Solids*, 2018, 496(9): 42-47.
13. Y Zhang, J Yao, X Y Zhao, et al. Ti substituted Ni-free $Zr_{65-x}Ti_xCu_5Fe_{10}Al_{7.5}$ bulk metallic glasses with significantly enhanced glass-forming ability and mechanical properties. *Journal of Alloys and*

Compounds, 2019, 773(1): 713-718.

14. J C Qiao, J Cong, Q Wang, et al. Effects of iron addition on the dynamic mechanical relaxation of $Zr_{55}Cu_{30}Ni_5Al_{10}$ bulk metallic glasses. *Journal of Alloys and Compounds*, 2018, 749(6): 262- 267.
15. K Sarlar, I Kucuk. Phase separation and glass forming ability of $(Fe_{72}Mo_{0.04}B_{0.24})_{100-x}Gd_x$ ($x=4,8$) bulk metallic glasses. *Journal of Non-Crystalline Solids*, 2016, 447(9): 198-201.
16. S Zheng, J W Li, J J Zhang, et al. Effect of Si addition on the electrochemical corrosion and passivation behavior of Fe-Cr-Mo-C-B-Ni-P metallic glasses. *Journal of Non-Crystalline Solids*, 2018, 493(8): 33-40.
17. B Escher, U Kühn, J Eckert, et al. Influence of Ag and Co additions on glass-forming ability, thermal and mechanical properties of Cu-Zr-Al bulk metallic glasses. *Materials Science & Engineering A*, 2016, 673(9): 90-98.
18. T H Chen, Y K Hsu. Mechanical properties and microstructural of biomedical Ti-based bulk metallic glass with Sn addition. *Computational Materials Science*, 2016, 117(5): 584-589.

Figures



Figure 1

Master alloy ingot



Figure 2

EONTEC 500-C vacuum pressure rapid prototyping equipment



Figure 3

Amorphous alloy sample

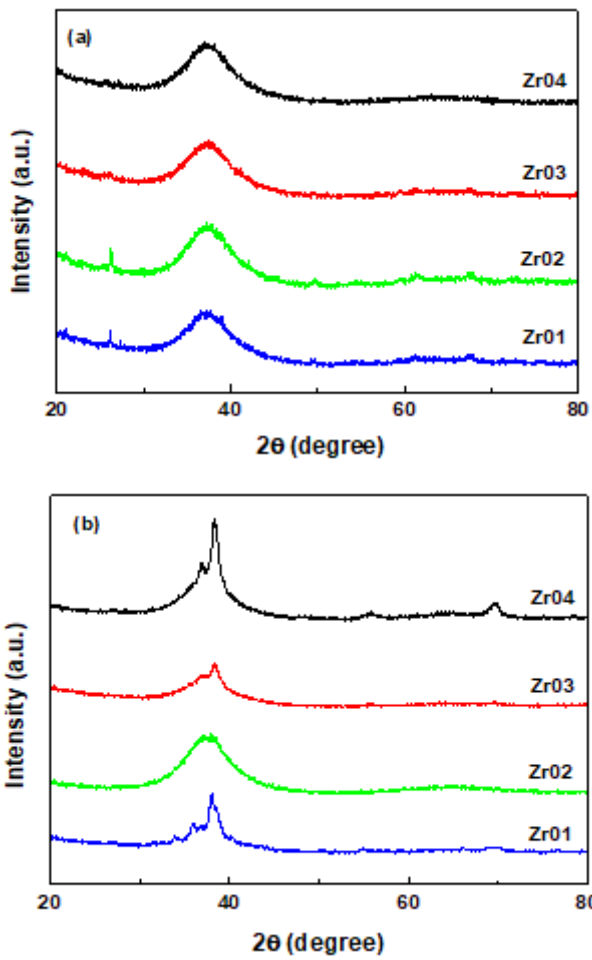


Figure 4

XRD pattern of samples with different thicknesses. (a) 1 mm thickness; (b) 2 mm thickness

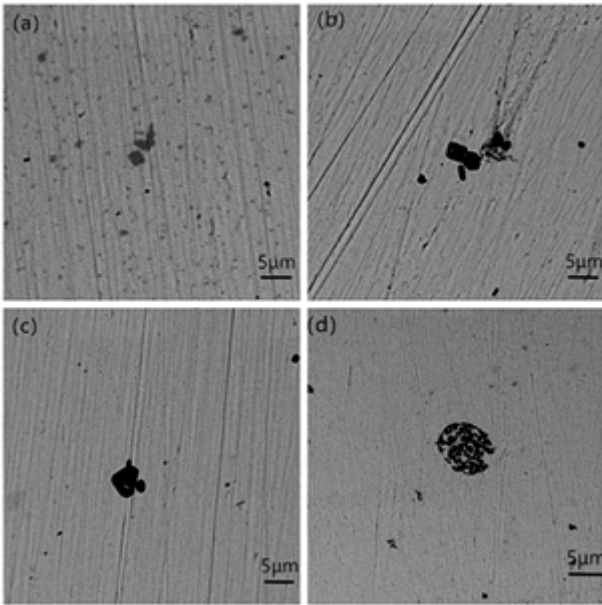


Figure 5

SEM images of $(\text{Zr}_{55}\text{Cu}_{30}\text{Al}_{10}\text{Ni}_5)_{100-x}\text{Sc}_x$ ($x = 0, 0.5, 1.0, 1.5$) alloys. (a) $x = 0$, (b) $x = 0.5$, (c) $x = 1.0$, (d) $x = 1.5$

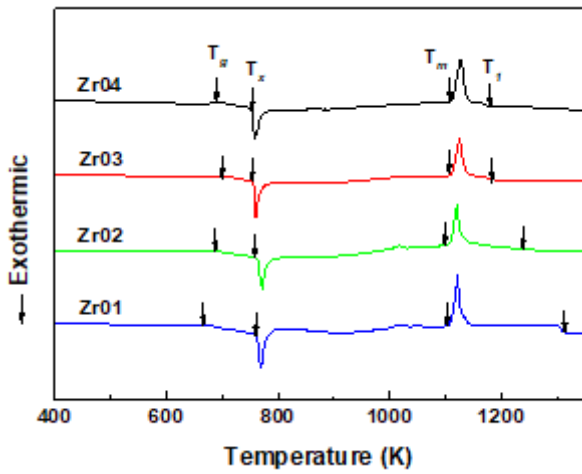


Figure 6

DSC curves of samples

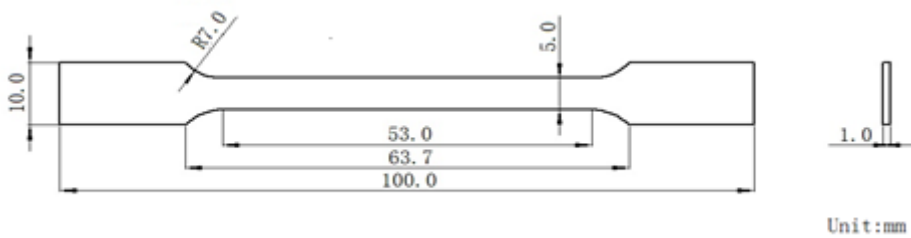


Figure 7

Uniaxial tensile conditions

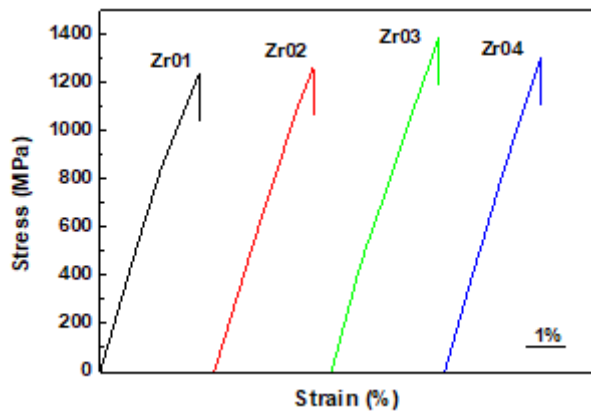


Figure 8

Tensile stress-strain curves of samples

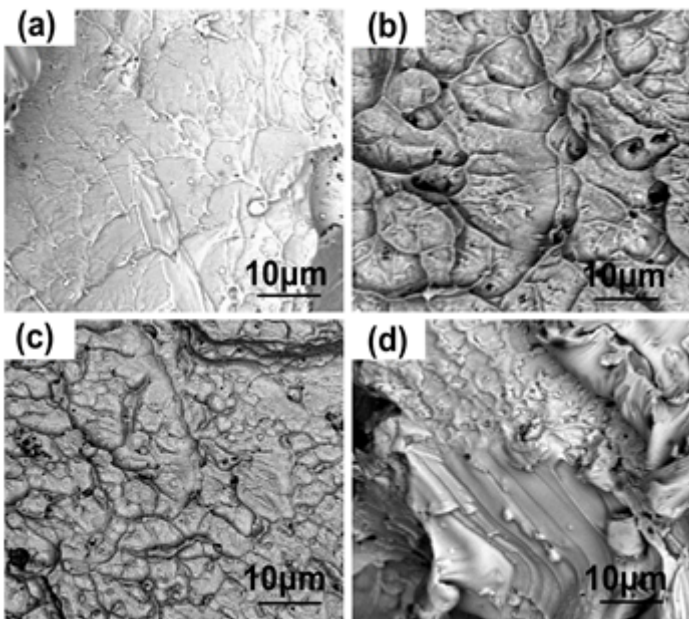


Figure 9

Fracture morphologies of (Zr55Cu30Al10Ni5)_{100-x}Sc_x (x = 0, 0.5, 1.0, 1.5) alloys. (a) x = 0, (b) x = 0.5, (c) x = 1.0, (d) x = 1.5

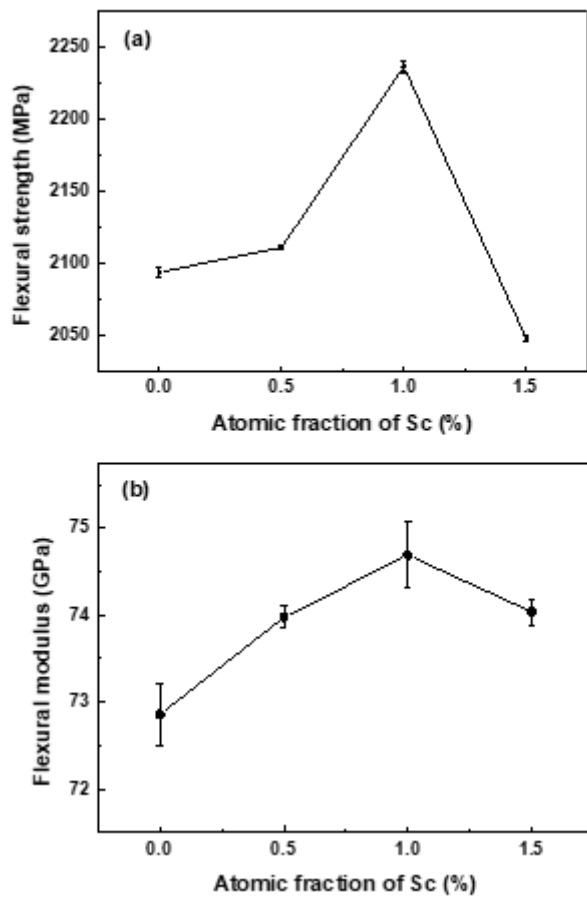
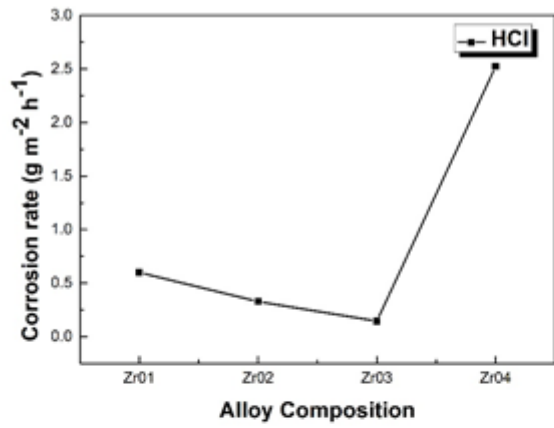
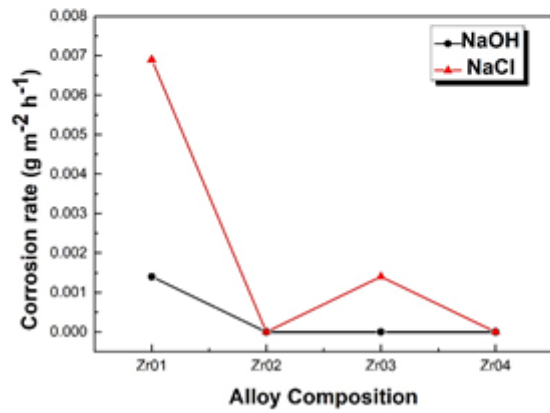


Figure 10

Flexural test results. (a) flexural strength versus atomic fraction of Sc; (b) flexural modulus versus atomic fraction of Sc



(a) In HCl solution



(b) In NaOH and NaCl solutions

Figure 11

Average corrosion rate of (Zr55Cu30Al10Ni5)100-xScx (x = 0, 0.5, 1.0, 1.5) alloys in HCl, NaOH, and NaCl solutions.